Wave-equation migration velocity analysis using plane-wave common-image gathers

Bowen Guo and Gerard T. Schuster

ABSTRACT

Wave-equation migration velocity analysis (WEMVA) based on subsurface-offset, angle domain, or time-lag common-image gathers (CIGs) requires significant computational and memory resources because it computes higher dimensional migration images in the extended image domain. To mitigate this problem, we have developed a WEMVA method using plane-wave CIGs. Plane-wave CIGs reduce computational cost and memory storage because they are directly calculated from prestack plane-wave migration and the number of plane waves is often much smaller than the number of shots. In the case of an inaccurate migration velocity, the moveout of plane-wave CIGs is automatically picked by a semblance analysis method, which is then linked to the migration velocity update by a connective function. Numerical tests on two synthetic data sets and a field data set validate the efficiency and effectiveness of this method.

INTRODUCTION

An accurate estimate of the velocity model is important to obtain focused images with migration. Two different categories of methods have been discussed extensively in the literature: data-domain methods, such as full-waveform inversion (FWI) (Tarantola, 1984; Pratt, 1999; Virieux and Operto, 2009), and image-domain methods, such as migration velocity analysis (MVA) (Stork, 1992; Biondi et al., 1999; Yilmaz, 2001; Mulder and Ten Kroode, 2002; Sava and Biondi, 2004; Shen and Symes, 2008). FWI inverts for the velocity model with high resolution, yet it suffers from the problem of local minima (Bunks et al., 1995) and often requires a good initial velocity model to converge to the correct velocity. MVA inverts for the migration velocity, which maximizes the similarities of a group of images, which is referred to as common-image gathers (CIGs). The inverted velocity model has moderate resolution and can then serve as the initial model for FWI. The assumption used by MVA is that using an accurate background velocity, the reflectors in the subsurface must be imaged at the same location for all the images, so that the CIGs are flat or focused. On the contrary, an inaccurate velocity will lead to shifts or defocusing between different images, and MVA back-projects the displacement or defocusing information to give the velocity update. The back-projection can be realized with either a ray-based operator (Stork, 1992; Yilmaz, 2001), or a wave-equation-based operator (Biondi et al., 1999; Mulder and Ten Kroode, 2002; Sava and Biondi, 2004; Shen and Symes, 2008). In general, wave-equation MVA (WEMVA) is intrinsically more robust than ray-based MVA because it avoids the high-frequency assumption in the ray-tracing method.

WEMVA can be implemented using CIGs in different domains such as the shot (Perrone et al., 2014), angle (Xu et al., 2001; Sava and Fomel, 2003; Biondi and Symes, 2004), subsurface-offset (Rickett and Sava, 2002), and time-lag domains (Sava and Fomel, 2006). Subsurface-offset and time-lag CIGs require an extended imaging condition in the space-lag and time-lag domains for each shot. Besides the physical dimensions in x-y-z, an extended image for a single shot has extra dimensions for space or time lags, which requires a significant increase in memory-storage space. Angle-domain CIGs are computed by a slant stack of the subsurface-offset CIGs (Sava and Fomel, 2003), or by calculating wavefield propagation directions during migration (Dickens and Winbow, 2011; Xu et al., 2011; Zhang, 2014). The final CIGs result from stacking all the shot gathers together. Computing these CIGs for WEMVA has a high computational cost and memory-storage requirement for large 3D data sets.

To mitigate this problem, plane-wave migration (Whitmore, 1995; Duquet et al., 2001; Zhang et al., 2005; Liu et al., 2006) can be applied to form plane-wave CIGs. This method combines multiple shot gathers into a composite plane-wave gather and migrates the plane-

wave gathers with different ray parameters p to obtain plane-wave CIGs. The benefit is that there is no need for the extra dimensions in the extended image domain. Moreover, the number of plane waves is often much smaller than the number of shots in the survey. Because of these two reasons, plane-wave CIGs save computational cost and memory space compared with CIGs in other domains.

Plane-wave technology has been used in the exploration geophysics community to save computational cost in FWI (Vigh and Starr, 2008) and least-squares migration (Dai and Schuster, 2013; Wang et al., 2014). Jiao et al. (2002) applied residual MVA in the plane-wave domain, in which the migration velocities were scanned and picked to flatten plane-wave CIGs by a moveout correction based on an analytical moveout formula. However, this formula is only valid for a 1D velocity model or a 2D model with small dip angles.

To overcome this limitation, we present a WEMVA method using plane-wave CIGs, denoted as PWEMVA. PWEMVA inverts for the migration velocity by finding the velocity model that minimizes the objective function, which is the squared summation of the local shifts between a plane-wave migration image and a reference image. The idea of defining the objective function as the local displacements between different images or data has been proposed to invert for the subsurface velocity model (Ma and Hale, 2013; Perrone et al., 2014, 2015), or the velocity variations associated with a 4D time-lapse seismic survey (Perrone and Sava, 2013). However, these methods still require a high computational cost because they compute images or data for every shot profile.

PWEMVA computes the local shift at a given image point by choosing a parabola that best fits the moveout of the plane-wave CIG. Similar approaches have been used by Zhang and Biondi (2013) and Zhang et al. (2015), except that they estimate the moveout of the shot and angle-domain CIGs. To compute the gradient of the objective function, we need to derive the Fréchet derivative of the local image shifts with respect to the migration velocity. This derivative is derived by using a connective function and the implicit function theorem (Luo and Schuster, 1991).

After the introduction, the "Theory" section summarizes the theory of plane-wave migration, introduces the PWEMVA objective function, and derives its gradient. The formula for updating the velocity model is given, and a workflow is presented for implementing the PWEMVA method. This is followed by the "Numerical results" section, which presents the results of applying PWEMVA to synthetic data and a marine data set recorded in the Gulf of Mexico. The last two sections include the discussions and conclusions.

THEORY

Plane-wave migration

For a 2D medium, let $S_k(\omega, \mathbf{x})$ represent the source-side wavefield of a single shot located at $(x_k, z = 0)$ at the surface. The plane-wave source-side wavefield $\bar{S}(\omega, \mathbf{x})$ is the summation of all the delayed shot wavefields from single shots:

$$\bar{S}(\omega, \mathbf{x}) = \sum_{k=1}^{n_s} e^{i\omega p(x_k - x_0)} S_k(\omega, \mathbf{x}), \quad (1)$$

where n_s represents the number of shots, i is the imaginary number, ω denotes the angular frequency, and $(x_0, 0)$ is the location at the surface where the plane wave is initiated at $t = 0$. Here, $p = \sin\theta/v$ is the ray parameter of the plane wave, where θ is referred to as the shooting angle and v is the velocity at the surface.

For the kth shot, the receiver-side wavefield $R_k(\omega, \mathbf{x})$ is calculated by backward extrapolation of the recorded data. Similar to equation 1, the plane-wave receiver-side wavefield $\bar{R}(\omega, \mathbf{x})$ is the summation of all the delayed $R_k(\omega, \mathbf{x})$:

$$\bar{R}(\omega, \mathbf{x}) = \sum_{k=1}^{n_s} e^{i\omega p(x_k - x_o)} R_k(\omega, \mathbf{x}). \quad (2)$$

A plane-wave gather can be seen as the plane-wave receiver wavefield at the receiver position $\mathbf{x}_g$. The terms $\bar{S}(\omega, \mathbf{x})$ and $\bar{R}(\omega, \mathbf{x})$ are functions of p, and, for simplicity, this dependence is omitted in the notation.

The prestack plane-wave migration image is obtained by multiplying the plane-wave source-side wavefield with the complex conjugate of the receiver-side wavefield in the frequency domain and summing over all frequencies:

$$m(\mathbf{x}) = \Re\left\{ \sum_{\omega} \bar{S}(\omega, \mathbf{x}) \bar{R}(\omega, \mathbf{x})^* \right\}, \quad (3)$$

where $\Re\{\}$ represents the real part.

Objective function and gradient

The objective function J for PWEMVA is defined as the summation of the squared vertical local shift $\Delta w_j(\mathbf{x}_o)$ between two patches $B(\mathbf{x}_o)$ (with the width and height of a wavelength) centered at $\mathbf{x}_o$ of a plane-wave migration image m_j and the reference image m_0:

$$J = \frac{1}{2} \sum_{j=1}^{n_p} \sum_{\mathbf{x}_o \in B} \Delta w_j(\mathbf{x}_o)^2, \quad (4)$$

where j denotes the plane-wave index, n_p represents the number of plane waves, and B stands for the set of all patches in the migration image. The local vertical shift $\Delta w_j(\mathbf{x}_o)$ aligns $m_0(x, z + \Delta w_j(\mathbf{x}_o))$ with $m_j(x, z)$ for $\mathbf{x} \in B(\mathbf{x}_o)$. In practice, the plane-wave image with the ray direction perpendicular to the subsurface structure is chosen to be the reference image. The details are further discussed in the "Workflow" section.

The gradient of the objective function with respect to the slowness $c(\mathbf{x}')$ (reciprocal of the migration velocity) is

$$\frac{\partial J}{\partial c(\mathbf{x}')} = \sum_{j=1}^{n_p} \sum_{\mathbf{x}_o \in B} \frac{\partial \Delta w_j(\mathbf{x}_o)}{\partial c(\mathbf{x}')} \Delta w_j(\mathbf{x}_o). \quad (5)$$

To calculate the Fréchet derivative of the local shift of the window centered at $\mathbf{x}_o$ with respect to the slowness perturbation at $\mathbf{x}'$, a connective function is defined as the local crosscorrelation between $m_0(B(\mathbf{x}_o))$ and $m_j(B(\mathbf{x}_o))$:

$$f_j(c(\mathbf{x}'), w_j(\mathbf{x}_o)) = \sum_{\mathbf{x} \in B(\mathbf{x}_o)} m_0(x, z + w_j(\mathbf{x}_o)) m_j(x, z), \quad (6)$$

where $\mathbf{x} = (x, z)$ and $w_j(\mathbf{x}_o)$ is an arbitrary local shift. The correct image shift $\Delta w_j(\mathbf{x}_o)$ aligns $m_0(x, z + \Delta w_j(\mathbf{x}_o))$ with $m_j(x, z)$ within $B(\mathbf{x}_o)$, so that the connective function in equation 6 is maximized. This means that the derivative of f_j with respect to $w_j(\mathbf{x}_o)$ should be zero at $\Delta w_j(\mathbf{x}_o)$:

$$\bar{f}_j(c(\mathbf{x}'),\Delta w_j(\mathbf{x}_o))=\sum_{\mathbf{x}\in B(\mathbf{x}_o)}\frac{\partial f_j(c(\mathbf{x}'),w_j(\mathbf{x}_o))}{\partial w_j(\mathbf{x}_o)}\bigg|_{w_j(\mathbf{x}_o)=\Delta w_j(\mathbf{x}_o)},$$

$$=\sum_{\mathbf{x}\in B(\mathbf{x}_o)}m_j(x,z)\dot{m}_0(x,z+\Delta w_j(\mathbf{x}_o)),$$

$$=0, \qquad (7)$$

where the dot represents the derivative with respect to z.

The implicit function theorem gives

$$\frac{\partial\Delta w_j(\mathbf{x}_o)}{\partial c(\mathbf{x}')}=-\frac{\partial\bar{f}_j/\partial c(\mathbf{x}')}{\partial\bar{f}_j/\partial\Delta w_j(\mathbf{x}_o)}, \qquad (8)$$

where the denominator is given by

$$\frac{\partial\bar{f}_j}{\partial\Delta w_j(\mathbf{x}_o)}=\sum_{\mathbf{x}\in B(\mathbf{x}_o)}\ddot{m}_0(x,z+\Delta w_j(\mathbf{x}_o))m_j(x,z).$$

$$(9)$$

Here, the double dots represent the second-order derivative with respect to z.

Assuming only m_j is a function of the migration slowness (this assumption is further discussed in the "Workflow" section), the numerator of equation 8 is

$$\frac{\partial\bar{f}_j}{\partial c(\mathbf{x}')}=\sum_{\mathbf{x}\in B(\mathbf{x}_o)}\dot{m}_0(x,z+\Delta w_j(\mathbf{x}_o))\frac{\partial m_j(\mathbf{x})}{\partial c(\mathbf{x}')}. \qquad (10)$$
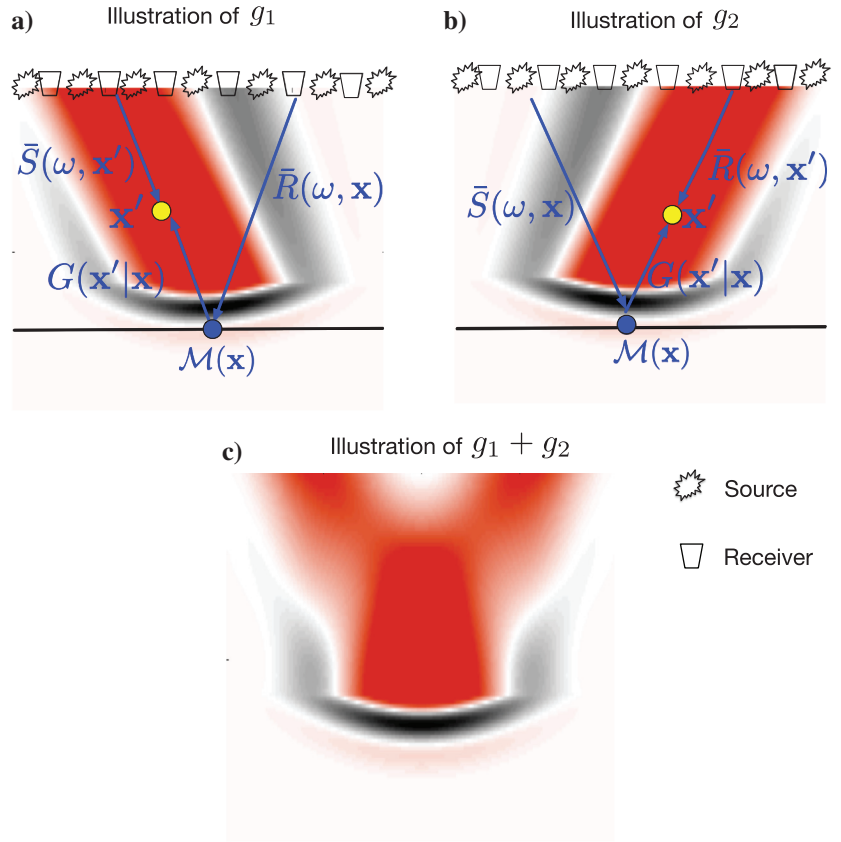

Figure 1. Wavepath diagrams illustrate (a) g_1, (b) g_2, and (c) g_1+g_2, where $\mathcal{M}(\mathbf{x})$ is an interface with a positive reflection coefficient as shown by the black horizontal line in (a and b).
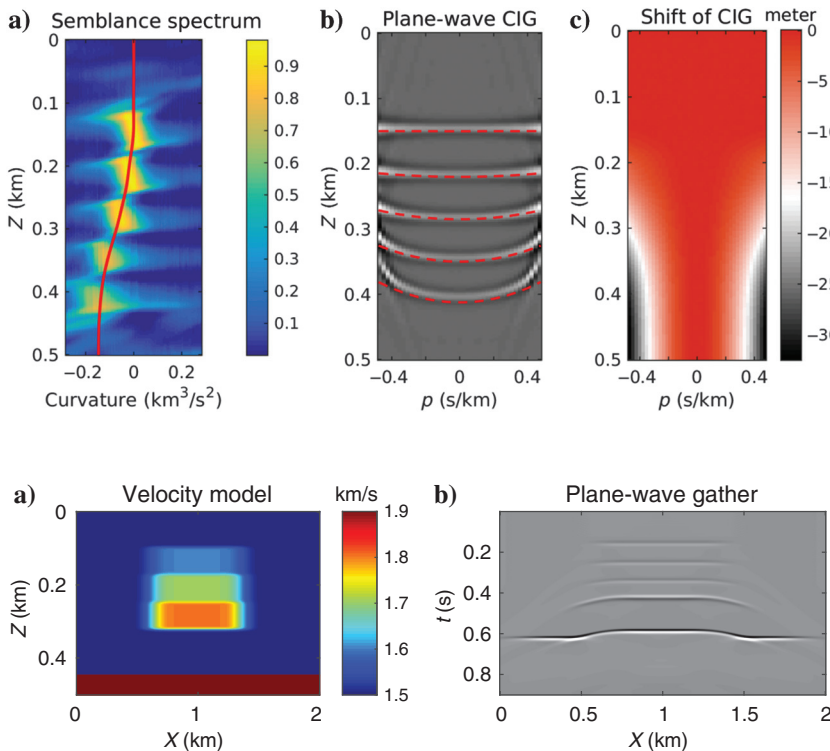

Figure 2. (a) A semblance spectrum calculated from (b) a plane-wave CIG. (c) The vertical shift of the CIG calculated from the picked curvature parameters in (a). The data are generated for a laterally homogeneous six-layer velocity model, and then migrated using a homogeneous velocity slower than the true velocity. The curvature parameters corresponding to the maximum energy of the spectrum are picked automatically as shown by the red line in (a) and then transformed into the shift values in (c). The dashed red lines in (b) represent the depth calculated from the shift values, which mostly agree with the depths of the migrated events.

Figure 3. (a) True velocity model and (b) the plane-wave gather with $p=0$.

Inserting equations 8–10 into equation 5 yields

$$\frac{\partial J}{\partial c(\mathbf{x}')} = \sum_{j=1}^{n_p} \sum_{\mathbf{x}_o \in B} \frac{-\sum_{\mathbf{x} \in B(\mathbf{x}_o)} \Delta w_j(\mathbf{x}_o) \dot{m}_0(x, z + \Delta w_j(\mathbf{x}_o)) \frac{\partial m_j(\mathbf{x})}{\partial c(\mathbf{x}')}}{\sum_{\mathbf{x} \in B(\mathbf{x}_o)} \dot{m}_0(x, z + \Delta w_j(\mathbf{x}_o)) m_j(\mathbf{x})}.$$

(11)

a)

CIGs using homogeneous velocity

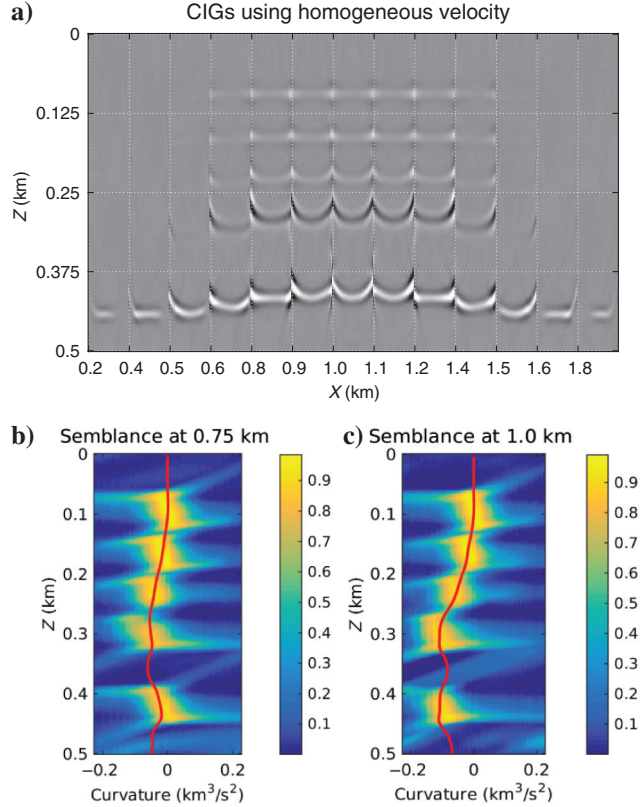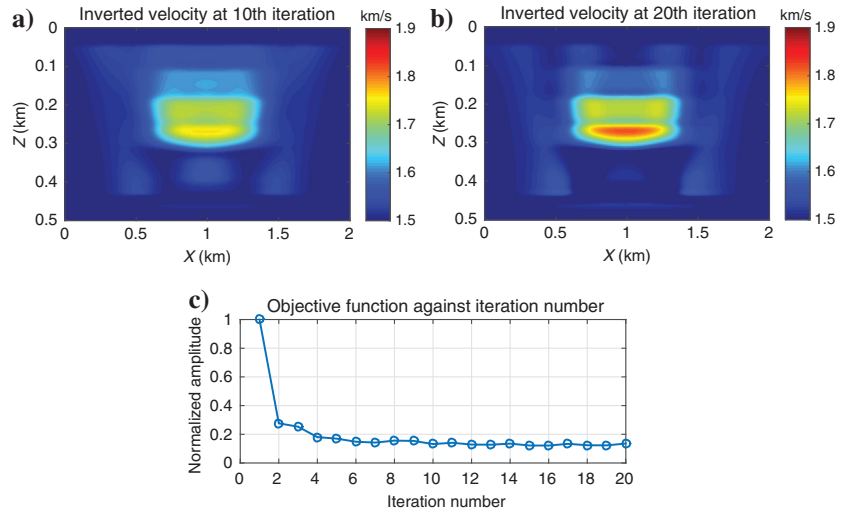**b)** Semblance at 0.75 km   **c)** Semblance at 1.0 km

Figure 4. (a) Plane-wave CIGs migrated with homogeneous velocity model. The calculated semblance spectra and the picked curvatures at 0.75 and 1 km are shown in (b and c).

Figure 5. (a) Inverted velocity models after 10 iterations and (b) 20 iterations. (c) The value of the objective function at each iteration.

Substituting the Fréchet derivative $\partial m_j(\mathbf{x})/\partial c(\mathbf{x}')$ derived in Appendix A into equation 11, the gradient of the objective function is

$$\frac{\partial J}{\partial c(\mathbf{x}')} = \sum_{j=1}^{n_p} \sum_{\mathbf{x}_o \in B} \frac{\sum_{\mathbf{x} \in B(\mathbf{x}_o)} g_1 + g_2}{\sum_{\mathbf{x} \in B(\mathbf{x}_o)} \ddot{m}_0(x, z + \Delta w_j(\mathbf{x}_o)) m_j(\mathbf{x})},$$ (12)

where $g_1 = \Re\left\{ \sum_\omega 2\omega^2 c(\mathbf{x}') \bar{S}(\omega, \mathbf{x}') \overbrace{\left[G(\mathbf{x}'|\mathbf{x})^* \mathcal{M}(\mathbf{x}) \bar{R}(\omega, \mathbf{x}) \right]}^{\text{upward-propagated receiver wavefield}}{}^* \right\}$,

and $g_2 = \Re\left\{ \sum_\omega 2\omega^2 c(\mathbf{x}') \overbrace{G(\mathbf{x}'|\mathbf{x}) \mathcal{M}(\mathbf{x}) \bar{S}(\omega, \mathbf{x})}^{\text{upward-propagated source wavefield}} \bar{R}(\omega, \mathbf{x}')^* \right\}$,

in which $\mathcal{M}(\mathbf{x}) = -\Delta w_j(\mathbf{x}_o) \dot{m}_0(x, z + \Delta w_j(\mathbf{x}_o))$, (13)

where $G(\mathbf{x}'|\mathbf{x})$ represents the Green's function recorded at $\mathbf{x}'$ due to a harmonic point source at $\mathbf{x}$ oscillating at a specific angular frequency ω. The gradient in equation 12 has two terms. The first term g_1 corresponds to the source-side wavepath, which is the dot product at $\mathbf{x}'$ between the downward-propagated source-side wavefield $\bar{S}(\omega, \mathbf{x}')$ and the upward-propagated receiver-side wavefield. The upward-propagated receiver-side wavefield is generated by a virtual source at the image point $\mathbf{x}$, which is redatumed from the receivers at the surface, as shown in Figure 1a. Similarly, the second term g_2 can be interpreted as the receiver-side wavepath, which is the dot product at $\mathbf{x}'$ between the downward-propagated receiver-side wavefield $\bar{R}(\omega, \mathbf{x}')$ and the upward-propagated source-side wavefield. The upward-propagated source-side wavefield is excited by a virtual source at the image point $\mathbf{x}$, which is redatumed from the sources at the surface, as shown in Figure 1b. The migration slowness is updated by smearing the energy of the local-image shifts at $\mathbf{x}$ along its plane-wave paths associated with the sources and receivers as shown in Figure 1c.

Equations 4–13 are for the vertical shifts between 2D images. More generally, the local shift between 3D images is a three-component vector, and the objective function in equation 4 can be generalized as the summation of the squared length of the shift vectors (Huang et al., 2014; Perrone et al., 2014, 2015; Perrone and Sava, 2015). In this case, the corresponding gradient with respect to the migration slowness is derived in Appendix B.

a) Inverted velocity at 10th iteration   **b)** Inverted velocity at 20th iteration

c) Objective function against iteration number

Given the gradient, the steepest-descent method (Nocedal and Wright, 2006) can be used to iteratively update the migration slowness until the shifts in plane-wave CIGs are sufficiently small. An alternative is the conjugate-gradient method (Nocedal and Wright, 2006).
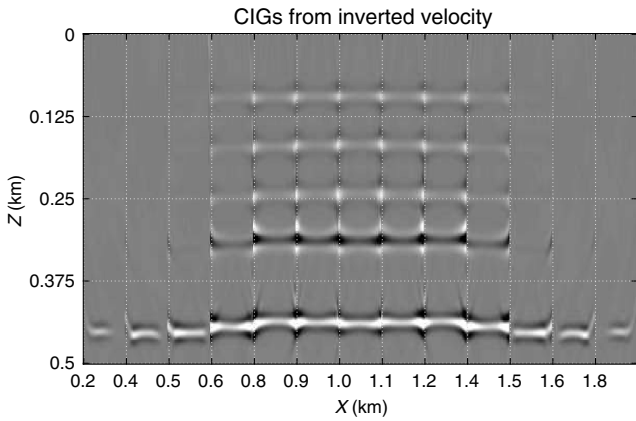

Figure 6. Plane-wave CIGs using the inverted velocity model shown in Figure 5b.
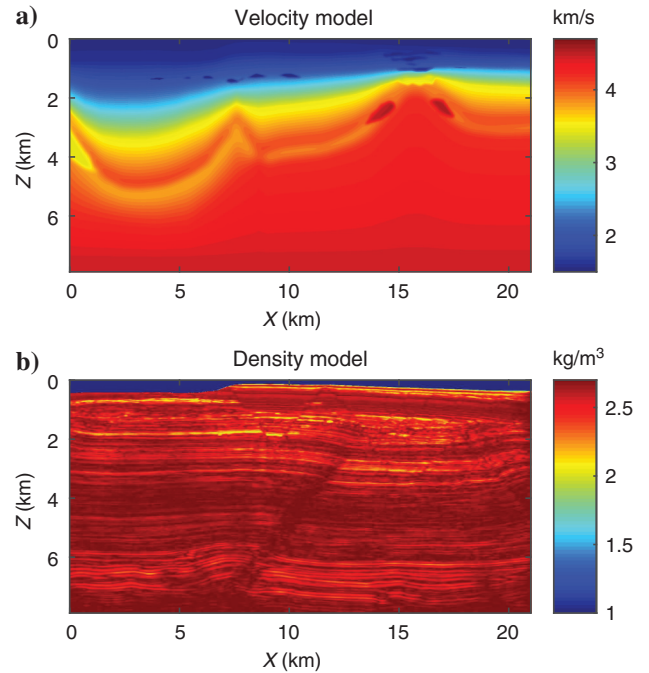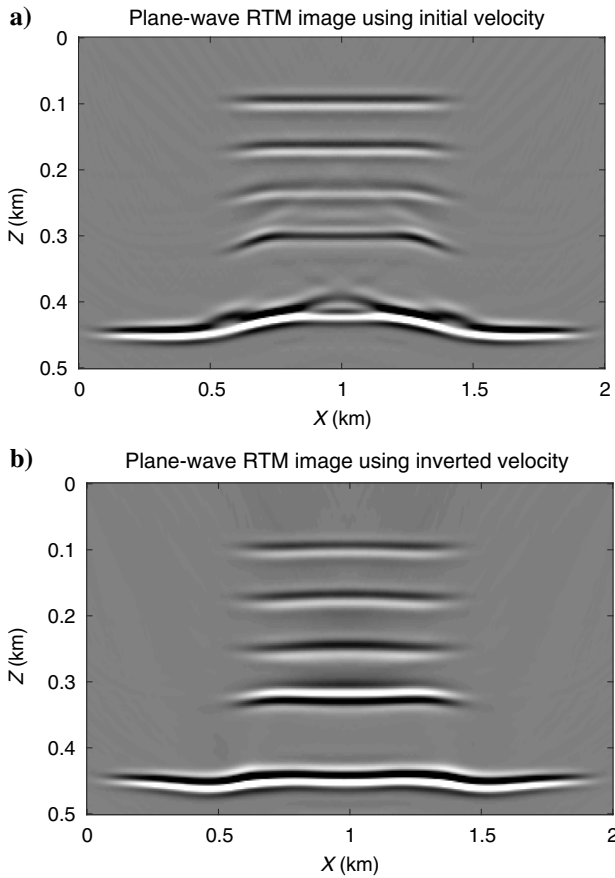

Figure 7. Stacked plane-wave RTM images (a) using the initial homogeneous velocity model and (b) using the inverted velocity model in Figure 5b.

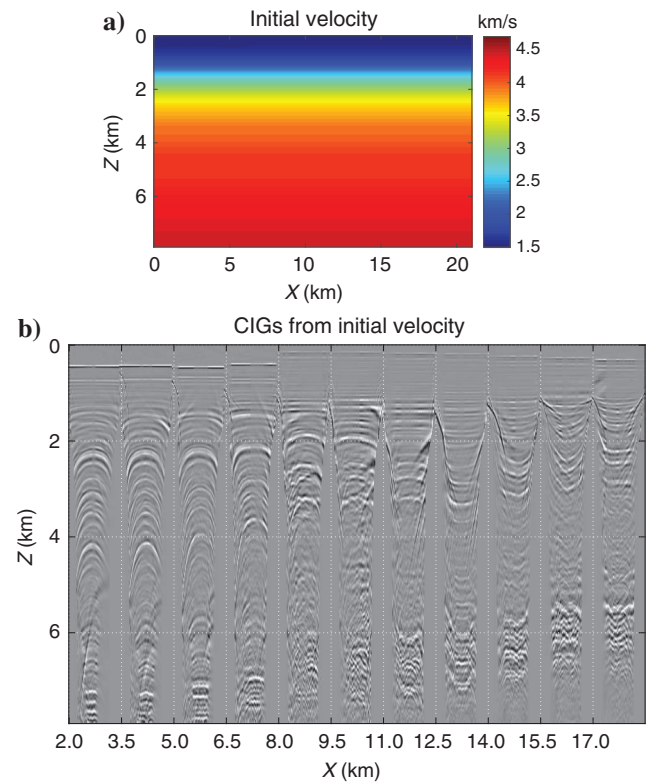Figure 8. (a) True velocity model and (b) true density model.

Figure 9. (a) Initial velocity model and (b) the associated plane-wave CIGs.

WORKFLOW

This section describes the workflow of the PWEMVA method, which is summarized by three steps: Calculate (1) the objective function, (2) the gradient, and (3) the step length. The implementation of the first two steps is now described in detail.

1) Calculate the objective function.

First, the shot profile data are transformed into plane-wave gathers based on equation 2. Then, plane-wave prestack reverse time migration (RTM) is applied to each plane-wave gather to obtain plane-wave CIGs. The poorly illuminated boundary areas of the migration images are masked.

The objective function in equation 4 requires calculating the local shifts between the same event in a plane-wave migration image and a reference image. In theory, the reference image is assumed to be invariant to migration velocity changes, and this assumption is only valid for the image migrated with an accurate velocity model. This is hardly feasible because the true velocity model is never known. In practice, the reference image is assumed to be the plane-wave migration image with the ray direction perpendicular to the subsurface structure because, for a moderate complex velocity, it usually suffers the least from velocity errors.

We use semblance analysis to calculate the shifts in the plane-wave CIGs. The semblance spectrum (Taner and Koehler, 1969; Neidell and Taner, 1971) is calculated by scanning over different curvatures α of a parabola to fit the plane-wave CIGs:

$$\Delta \tilde{w}_j(\mathbf{x}) = \alpha p^2, \tag{14}$$

where $\Delta \tilde{w}_j(x, z)$ is the local shift that aligns $m_0(x, z)$ with $m_j(x, z + \Delta \tilde{w}_j(x, z))$. The function $\Delta \tilde{w}_j(x, z)$ can then be transformed into $\Delta w_j(x, z)$ by
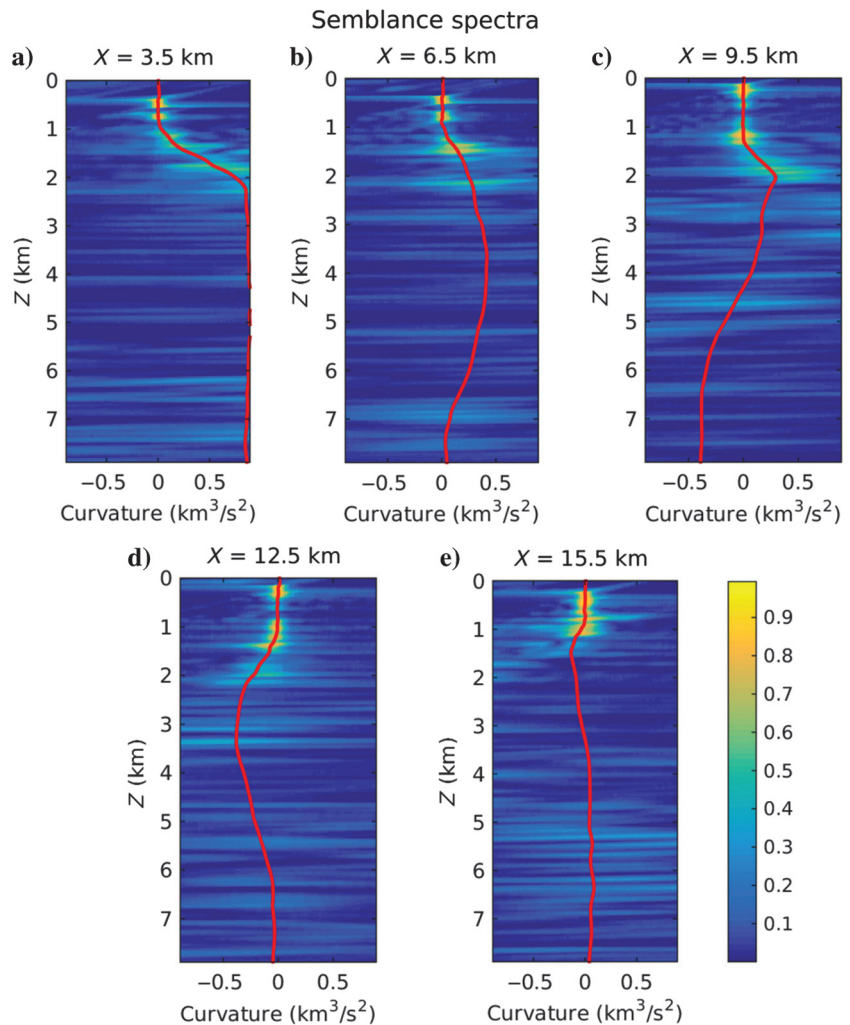
$$\Delta w_j(x, z) = -\Delta \tilde{w}_j(x, z - \Delta \tilde{w}_j(x, z)). \tag{15}$$

The reason for fitting the plane-wave CIG with a parabola is explained in Appendix C. However, equation 14 implicitly assumes the apex of the parabola at the image with $p = 0$, and this is not accurate for a large dip-angle interface. In this case, equation 14 is replaced with

$$\Delta \tilde{w}_j(\mathbf{x}) = \alpha(p - p_0)^2, \quad \text{where } p_0 = \sin \beta / v(\mathbf{x}), \tag{16}$$

in which p_0 is the ray parameter of the plane wave reflecting perpendicularly off the interface dipping at an angle β and $v(\mathbf{x})$

Figure 10. Semblance spectra at (a) $x = 3.5$ km, (b) $x = 6.5$ km, (c) $x = 9.5$ km, (d) $x = 12.5$ km, and (e) $x = 15.5$ km. The red lines represent the picked curvatures of the maximum energy.

is the migration velocity at **x**. The value of β can be computed from the migration image.

After calculating the semblance spectrum, the curvature corresponding to the maximum energy is automatically picked
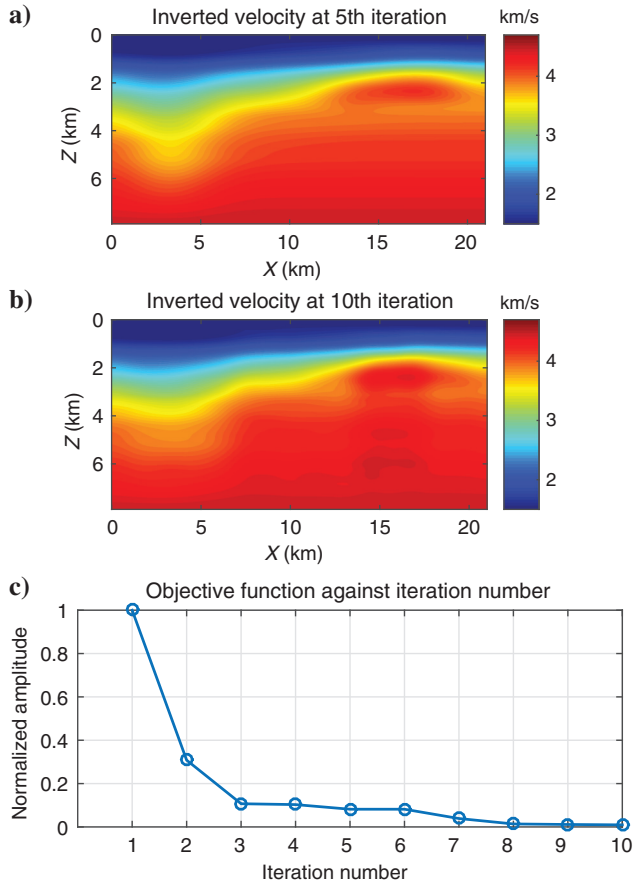

a)

b)

c)

Figure 11. Inverted velocity model after (a) five iterations and (b) 10 iterations. Panel (c) plots the value of the objective function at each iteration.
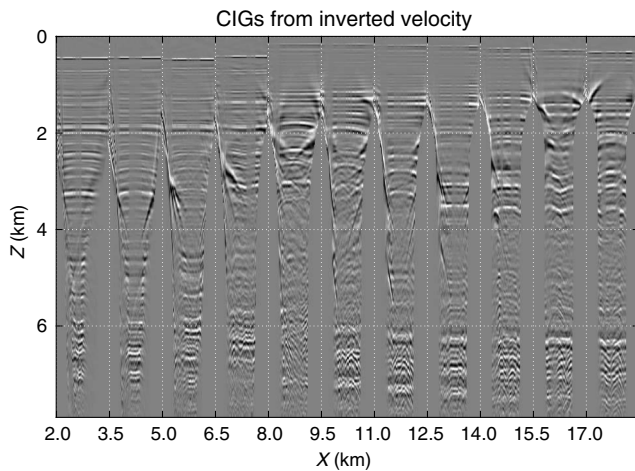

Figure 12. Plane-wave CIGs using the inverted velocity model shown in Figure 11b.

using the method proposed by Fomel (2009). As an example, Figure 2a shows a semblance spectrum computed from a plane-wave CIG shown in Figure 2b, and the picked curvature parameters are then transformed into the shift based on equation 14 or 16, as shown in Figure 2c.

2) Calculate the gradient.

When calculating the gradient, equation 13 is simplified as

$$\mathcal{M}(\mathbf{x}) = -\Delta w_j(\mathbf{x}_o)\dot{m}_j(\mathbf{x}), \qquad (17)$$

by assuming $\dot{m}_0(x, z + \Delta w_j(\mathbf{x}_o)) \approx \dot{m}_j(x, z)$. The denominator of equation 12 is also omitted in implementation because dividing an image can be unstable.

The Green's functions in equation 12 are computed by solving the two-way acoustic-wave equation in the time domain, whereas the background slowness model needs to be smoothed to avoid reflection events in the Green's functions.

3) Given the gradient, a numerical line-search method is used to calculate the step length and update the slowness model by the steepest-descent or the conjugate-gradient methods (Nocedal and Wright, 2006).

NUMERICAL RESULTS

The PWEMVA method is applied to two synthetic data sets and a marine data set recorded in the Gulf of Mexico. These tests are designed to demonstrate the strengths and limitations of this velocity-analysis method.
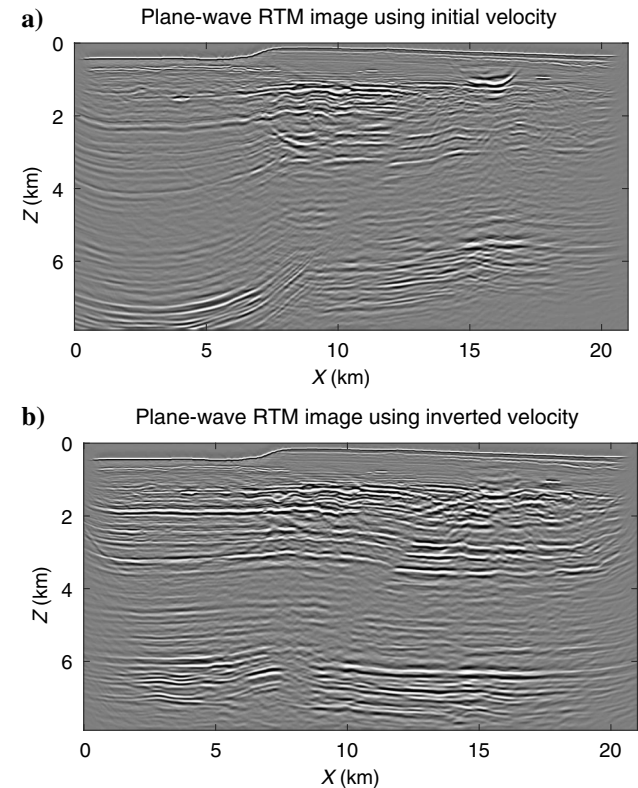

a)

b)

Figure 13. Stacked plane-wave RTM images (a) using the initial velocity model in Figure 9a and (b) using the inverted velocity model in Figure 11b.

Synthetic test 1

The PWEMVA method is first tested on the data generated for a simple 2D model, which is 2 km wide and 0.5 km deep. Synthetic shot gathers are computed by finite-difference solutions to the 2D acoustic-wave equation for the velocity model shown in Figure 3a. The source wavelet is a Ricker wavelet with a 40-Hz peak frequency, and there are 201 shots with 402 active receivers per shot. The sources and receivers are evenly distributed on the surface with intervals of 10 and 5 m, respectively. The shot profile data are transformed into 41 plane-wave gathers with -0.471 s/km $\leq p \leq 0.471$ s/km and shooting angles changing from $-45°$ to $45°$. The plane-wave gather with $p = 0$ is shown in Figure 3b, and the initial velocity model is homogeneous with $v = 1.5$ km/s. These CIGs using the initial velocity model are shown in Figure 4a. The semblance spectra and the moveout residuals computed from the CIGs at two locations are shown in Figure 4b and 4c. The inverted velocity models after 10 and 20 iterations are shown in Figure 5a and 5b, respectively, in which the final tomogram accurately resembles the true velocity model. Figure 5c depicts the values of the objective function at each iteration, and the plane-wave CIGs shown in Figure 6 are mostly flattened using the inverted velocity model after 20 iterations. We also compare the stacked plane-wave images using the homogeneous and inverted velocity models in Figure 7. It is evident that the inverted velocity model produces more focused and flatter image. For the deepest reflector, the minor distortions shown in Figure 7b and the slight curvatures in Figure 6 are due to the circular bottom and the vertical artifacts at $x = 0.5$ and
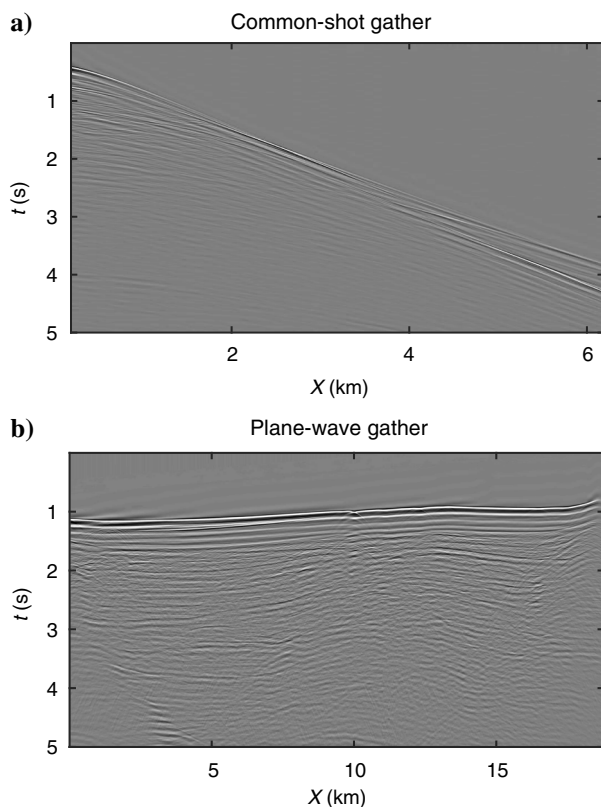
1.5 km of the inverted velocity model in Figure 5b. These errors are the results of uneven illumination and the velocity/depth ambiguity (Bickel, 1990; Ross, 1994).

Synthetic test 2

The second test inverts the synthetic data generated by a staggered-grid acoustic modeling algorithm. The velocity and density models are shown in Figure 8 with the width of 21 km and the depth of 7.9 km taken from a portion of the BP2004 model. The source wavelet is a Ricker wavelet with a 15-Hz peak frequency. There are 690 shots with 2070 receivers per shot. The shots and receivers are evenly distributed on the surface at 30 and 10 m intervals, respectively. These data are transformed into 81 plane-wave gathers with the ray parameters ranging from -0.33 to 0.33 s/km and the shooting angles varying from $-30°$ to $30°$. The laterally homogeneous velocity model shown in Figure 9a is the initial velocity, which produces the plane-wave CIGs with strong residual moveouts between 2–8 km and 12.5–15.5 km along the horizontal distance as shown in Figure 9b. Figure 10 depicts the semblance spectra and the picked curvatures at different horizontal locations. The velocity of the water layer is not updated in the inversion.

The inverted velocity models after five and 10 iterations are shown in Figure 11a and 11b, respectively. After 10 iterations, the tomogram recovers most of the low-wavenumber components of the true-velocity model in Figure 8a. Figure 11c shows the values of the objective function at each iteration, and the plane-wave CIGs associated with the inverted velocity after 10 iterations are mostly flattened as shown in Figure 12. We now compare the stacked plane-wave images in Figure 13 using the initial and inverted veloc-

a)

b)

Figure 14. (a) A CSG recorded in the Gulf of Mexico data and (b) a plane-wave gather with $p = -0.04$ s/km.
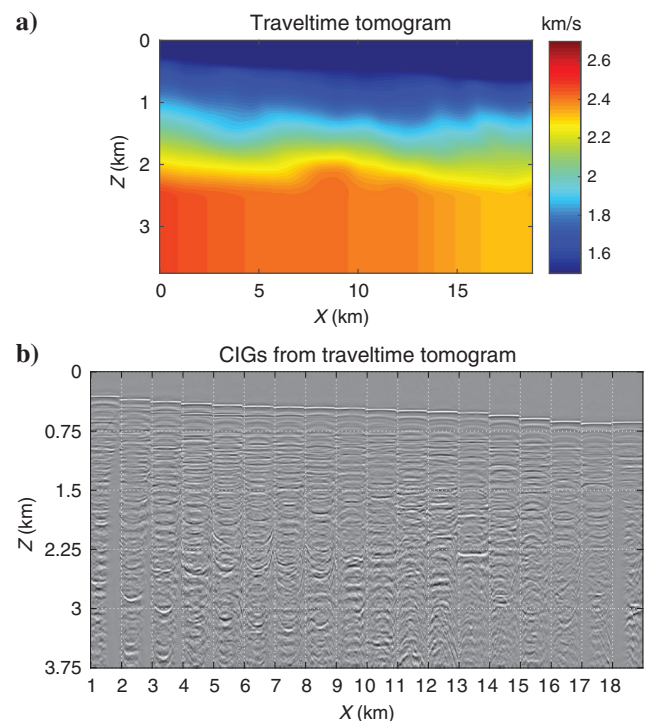
a)

b)

Figure 15. (a) The initial velocity model computed by inverting the traveltimes of the first arrivals and (b) the associated plane-wave CIGs.

The perturbed Green's function $\Delta G(\mathbf{x}|\mathbf{x}_k)$ can be expressed under the Born approximation as

$$\Delta G(\mathbf{x}|\mathbf{x}_k) = \int 2\omega^2 c(\mathbf{x}'') G(\mathbf{x}|\mathbf{x}'') G(\mathbf{x}''|\mathbf{x}_k) \Delta c(\mathbf{x}'') d\mathbf{x}'', \tag{A-5}$$

where $\Delta c(\mathbf{x}'')$ is the slowness perturbation. Assuming

$$\Delta c(\mathbf{x}'') = \Delta c \delta(\mathbf{x}'' - \mathbf{x}'), \tag{A-6}$$

we obtain

$$\frac{\partial G(\mathbf{x}|\mathbf{x}_k)}{\partial c(\mathbf{x}')} = 2\omega^2 c(\mathbf{x}') G(\mathbf{x}|\mathbf{x}') G(\mathbf{x}'|\mathbf{x}_k). \tag{A-7}$$

Substituting the combination of equations A-4 and A-7 into the expression of γ_1 in equation A-1 yields

$$\gamma_1 = \Re\left\{ \sum_{\omega} 2\omega^2 c(\mathbf{x}') W(\omega) \sum_{k=1}^{n_s} e^{i\omega p(x_k - x_o)} G(\mathbf{x}'|\mathbf{x}_k) G(\mathbf{x}|\mathbf{x}') \bar{R}(\omega,\mathbf{x})^* \right\}. \tag{A-8}$$

Inserting equations 1 and A-3 into equation A-8 and using the reciprocity property of the Green's function $G(\mathbf{x}|\mathbf{x}') = G(\mathbf{x}'|\mathbf{x})$, equation A-8 is simplified as

$$\gamma_1 = \Re\left\{ \sum_{\omega} 2\omega^2 c(\mathbf{x}') \bar{S}(\omega,\mathbf{x}') [G(\mathbf{x}'|\mathbf{x})^* \bar{R}(\omega,\mathbf{x})]^* \right\}. \tag{A-9}$$

The formula for γ_2 is derived in a similar way. Based on equation 2

$$\frac{\partial \bar{R}(\omega,\mathbf{x})}{\partial c(\mathbf{x}')} = \sum_{k=1}^{n_s} e^{i\omega p(x_k - x_o)} \frac{\partial R_k(\omega,\mathbf{x})}{\partial c(\mathbf{x}')}, \tag{A-10}$$

and

$$R_k(\omega,\mathbf{x}) = \sum_{\mathbf{x}_g} G(\mathbf{x}|\mathbf{x}_g)^* d(\omega,\mathbf{x}_g,\mathbf{x}_k), \tag{A-11}$$

where $R_k(\omega,\mathbf{x})$ is the backward extrapolated wavefield computed by the time-reversed propagation of the data $d(\omega,\mathbf{x}_g,\mathbf{x}_k)$ recorded at $\mathbf{x}_g$ excited by the source at $\mathbf{x}_k$.

Similar to equation A-7, Born modeling gives

$$\frac{\partial G(\mathbf{x}|\mathbf{x}_g)}{\partial c(\mathbf{x}')} = 2\omega^2 c(\mathbf{x}') G(\mathbf{x}|\mathbf{x}') G(\mathbf{x}'|\mathbf{x}_g). \tag{A-12}$$

Substituting equations A-11 and A-12 into equation A-10 gives

$$\begin{aligned}
\frac{\partial \bar{R}(\omega,\mathbf{x})}{\partial c(\mathbf{x}')} &= \sum_{k=1}^{n_s} e^{i\omega p(x_k - x_o)} 2\omega^2 c(\mathbf{x}') G(\mathbf{x}|\mathbf{x}')^* \\
&\quad \times \sum_{\mathbf{x}_g} G(\mathbf{x}'|\mathbf{x}_g)^* d(\omega,\mathbf{x}_g,\mathbf{x}_k), \\
&= 2\omega^2 c(\mathbf{x}') G(\mathbf{x}|\mathbf{x}')^* \bar{R}(\omega,\mathbf{x}'). \tag{A-13}
\end{aligned}$$

Inserting equation A-13 into the expression of γ_2 in equation A-1 and using the reciprocity property $G(\mathbf{x}|\mathbf{x}') = G(\mathbf{x}'|\mathbf{x})$ yields

$$\gamma_2 = \Re\left\{ \sum_{\omega} 2\omega^2 c(\mathbf{x}') [\bar{S}(\omega,\mathbf{x}) G(\mathbf{x}'|\mathbf{x})] \bar{R}(\omega,\mathbf{x}')^* \right\}. \tag{A-14}$$

Summarizing the previous derivations, we have

$$\frac{\partial m(\mathbf{x})}{\partial c(\mathbf{x}')} = \gamma_1 + \gamma_2, \quad \text{where}$$

$$\gamma_1 = \Re\left\{ \sum_{\omega} 2\omega^2 c(\mathbf{x}') \bar{S}(\omega,\mathbf{x}') [G(\mathbf{x}'|\mathbf{x})^* \bar{R}(\omega,\mathbf{x})]^* \right\},$$

$$\text{and} \quad \gamma_2 = \Re\left\{ \sum_{\omega} 2\omega^2 c(\mathbf{x}') [\bar{S}(\omega,\mathbf{x}) G(\mathbf{x}'|\mathbf{x})] \bar{R}(\omega,\mathbf{x}')^* \right\}. \tag{A-15}$$

APPENDIX B

EXTENSION OF THE OBJECTIVE FUNCTION AND GRADIENT TO THREE DIMENSIONS

The local shift between two small cubes $B(\mathbf{x}_o)$ centered at $\mathbf{x}_o$ of a 3D plane-wave migration image $m_j(\mathbf{x})$ and a reference image $m_0(\mathbf{x})$ is a three-component vector $\Delta\mathbf{u}_j(\mathbf{x}_o) = (\Delta u_j(\mathbf{x}_o), \Delta v_j(\mathbf{x}_o), \Delta w_j(\mathbf{x}_o))$, where Δu_j, Δv_j, and Δw_j are the components in the x-, y-, and z-directions, respectively. Similar to equation 4, the objective function is defined as

$$J = \frac{1}{2} \sum_{j=1}^{n_p} \sum_{\mathbf{x}_o \in B} \|\Delta\mathbf{u}_j(\mathbf{x}_o)\|^2, \tag{B-1}$$

where $\|\|$ denotes the length of the vector. The local-shift vector $\Delta\mathbf{u}_j(\mathbf{x}_o)$ aligns $m_0(\mathbf{x} + \Delta\mathbf{u}_j(\mathbf{x}_o))$ with $m_j(\mathbf{x})$ for $\mathbf{x} \in B(\mathbf{x}_o)$, where the size of $B(\mathbf{x}_o)$ is a wavelength. The gradient of the objective function with respect to the migration slowness $c(\mathbf{x}')$ is

$$\begin{aligned}
\frac{\partial J}{\partial c(\mathbf{x}')} &= \sum_{j=1}^{n_p} \sum_{\mathbf{x}_o \in B} \left\{ \frac{\partial \Delta u_j(\mathbf{x}_o)}{\partial c(\mathbf{x}')} \Delta u_j(\mathbf{x}_o) \right. \\
&\left. + \frac{\partial \Delta v_j(\mathbf{x}_o)}{\partial c(\mathbf{x}')} \Delta v_j(\mathbf{x}_o) + \frac{\partial \Delta w_j(\mathbf{x}_o)}{\partial c(\mathbf{x}')} \Delta w_j(\mathbf{x}_o) \right\}. \tag{B-2}
\end{aligned}$$

The connective function is defined as

$$f_j(c(\mathbf{x}'), \mathbf{u}_j(\mathbf{x}_o)) = \sum_{\mathbf{x} \in B(\mathbf{x}_o)} m_0(\mathbf{x} + \mathbf{u}_j(\mathbf{x}_o)) m_j(\mathbf{x}), \tag{B-3}$$

where $\mathbf{u}_j(\mathbf{x}_o)$ is an arbitrary local-shift vector. The correct image shift $\Delta\mathbf{u}_j(\mathbf{x}_o)$ aligns $m_0(\mathbf{x} + \Delta\mathbf{u}_j(\mathbf{x}_o))$ with $m_j(\mathbf{x})$. This means that the gradient of f_j with respect to $\mathbf{u}_j(\mathbf{x}_o)$ should be zero at $\Delta\mathbf{u}_j(\mathbf{x}_o)$:

$$
\begin{aligned}
\bar{\mathbf{f}}_j(c(\mathbf{x}'),\Delta\mathbf{u}_j(\mathbf{x}_o)) &= \nabla f_j(c(\mathbf{x}'),\mathbf{u}_j(\mathbf{x}_o))|_{\mathbf{u}_j(\mathbf{x}_o)=\Delta\mathbf{u}_j(\mathbf{x}_o)}, \\
&= (\overline{fx}_j,\overline{fy}_j,\overline{fz}_j), \\
&= \sum_{\mathbf{x}\in B(\mathbf{x}_o)} m_j(\mathbf{x})\left(\frac{\partial m_0(\mathbf{x}+\Delta\mathbf{u}_j(\mathbf{x}_o))}{\partial x},\right. \\
&\quad \left.\frac{\partial m_0(\mathbf{x}+\Delta\mathbf{u}_j(\mathbf{x}_o))}{\partial y},\frac{\partial m_0(\mathbf{x}+\Delta\mathbf{u}_j(\mathbf{x}_o))}{\partial z}\right), \\
&= (0,0,0). \qquad\qquad\qquad\qquad\qquad (\text{B-4})
\end{aligned}
$$

From the implicit function theorem, we have

$$
\begin{pmatrix}
\frac{\partial\Delta u_j(\mathbf{x}_o)}{\partial c(\mathbf{x}')} \\
\frac{\partial\Delta v_j(\mathbf{x}_o)}{\partial c(\mathbf{x}')} \\
\frac{\partial\Delta w_j(\mathbf{x}_o)}{\partial c(\mathbf{x}')}
\end{pmatrix}
= -
\begin{pmatrix}
\frac{\partial\overline{fx}_j}{\partial\Delta u_j(\mathbf{x}_o)} & \frac{\partial\overline{fx}_j}{\partial\Delta v_j(\mathbf{x}_o)} & \frac{\partial\overline{fx}_j}{\partial\Delta w_j(\mathbf{x}_o)} \\
\frac{\partial\overline{fy}_j}{\partial\Delta u_j(\mathbf{x}_o)} & \frac{\partial\overline{fy}_j}{\partial\Delta v_j(\mathbf{x}_o)} & \frac{\partial\overline{fy}_j}{\partial\Delta w_j(\mathbf{x}_o)} \\
\frac{\partial\overline{fz}_j}{\partial\Delta u_j(\mathbf{x}_o)} & \frac{\partial\overline{fz}_j}{\partial\Delta v_j(\mathbf{x}_o)} & \frac{\partial\overline{fz}_j}{\partial\Delta w_j(\mathbf{x}_o)}
\end{pmatrix}^{-1}
\begin{pmatrix}
\frac{\partial\overline{fx}_j}{\partial c(\mathbf{x}')} \\
\frac{\partial\overline{fy}_j}{\partial c(\mathbf{x}')} \\
\frac{\partial\overline{fz}_j}{\partial c(\mathbf{x}')}
\end{pmatrix}.
$$
$$(\text{B-5})$$

Inserting the expressions of $\overline{fx}_j$, $\overline{fy}_j$, and $\overline{fz}_j$ in equation B-4 into equation B-5 yields

$$
\begin{pmatrix}
\frac{\partial\Delta u_j(\mathbf{x}_o)}{\partial c(\mathbf{x}')} \\
\frac{\partial\Delta v_j(\mathbf{x}_o)}{\partial c(\mathbf{x}')} \\
\frac{\partial\Delta w_j(\mathbf{x}_o)}{\partial c(\mathbf{x}')}
\end{pmatrix}
= -A^{-1}
\begin{pmatrix}
\sum_{\mathbf{x}\in B(\mathbf{x}_o)}\frac{\partial m_j(\mathbf{x})}{\partial c(\mathbf{x}')}\frac{\partial m_0(\mathbf{x}+\Delta\mathbf{u}_j(\mathbf{x}_o))}{\partial x} \\
\sum_{\mathbf{x}\in B(\mathbf{x}_o)}\frac{\partial m_j(\mathbf{x})}{\partial c(\mathbf{x}')}\frac{\partial m_0(\mathbf{x}+\Delta\mathbf{u}_j(\mathbf{x}_o))}{\partial y} \\
\sum_{\mathbf{x}\in B(\mathbf{x}_o)}\frac{\partial m_j(\mathbf{x})}{\partial c(\mathbf{x}')}\frac{\partial m_0(\mathbf{x}+\Delta\mathbf{u}_j(\mathbf{x}_o))}{\partial z}
\end{pmatrix},
$$

where $A = \sum_{\mathbf{x}\in B(\mathbf{x}_o)} m_j(\mathbf{x})$

$$
\times
\begin{pmatrix}
\frac{\partial^2 m_0(\mathbf{x}+\Delta\mathbf{u}_j(\mathbf{x}_o))}{\partial x^2} & \frac{\partial^2 m_0(\mathbf{x}+\Delta\mathbf{u}_j(\mathbf{x}_o))}{\partial x\partial y} & \frac{\partial^2 m_0(\mathbf{x}+\Delta\mathbf{u}_j(\mathbf{x}_o))}{\partial x\partial z} \\
\frac{\partial^2 m_0(\mathbf{x}+\Delta\mathbf{u}_j(\mathbf{x}_o))}{\partial y\partial x} & \frac{\partial^2 m_0(\mathbf{x}+\Delta\mathbf{u}_j(\mathbf{x}_o))}{\partial y^2} & \frac{\partial^2 m_0(\mathbf{x}+\Delta\mathbf{u}_j(\mathbf{x}_o))}{\partial y\partial z} \\
\frac{\partial^2 m_0(\mathbf{x}+\Delta\mathbf{u}_j(\mathbf{x}_o))}{\partial z\partial x} & \frac{\partial^2 m_0(\mathbf{x}+\Delta\mathbf{u}_j(\mathbf{x}_o))}{\partial z\partial y} & \frac{\partial^2 m_0(\mathbf{x}+\Delta\mathbf{u}_j(\mathbf{x}_o))}{\partial z^2}
\end{pmatrix}. \qquad (\text{B-6})
$$

Substituting equation B-6 into equation B-2 gives the gradient of the objective function in equation B-1.

APPENDIX C

MOVEOUT ANALYSIS OF PLANE-WAVE CIGS

For a stack of N horizontal layers, Jiao et al. (2002) show that the migration image depth $z_N^m(p)$ of the plane-wave gather with the ray parameter p is

$$
z_N^m(p) = \sum_{i=1}^{N}\Delta z_i^t\frac{\sqrt{(c_i^t)^2 - p^2}}{\sqrt{(c_i^m)^2 - p^2}}, \qquad (\text{C-1})
$$

where c_i^t (c_i^m) represents the correct (incorrect) migration slowness at the ith layer.

Using the Taylor expansion and truncating after the second term gives

$$
\frac{\sqrt{(c_i^t)^2 - p^2}}{\sqrt{(c_i^m)^2 - p^2}} \approx \alpha_i^{(0)} + \alpha_i^{(2)}p^2, \qquad (\text{C-2})
$$

where

$$
\alpha_i^{(0)} = c_i^t/c_i^m,
$$

and $\alpha_i^{(2)} = \dfrac{1}{2(c_i^m)^2}\left(\dfrac{c_i^t}{c_i^m} - \dfrac{c_i^m}{c_i^t}\right)$. $\qquad (\text{C-3})$

Substituting equation C-2 into equation C-1 yields

$$
z_N^m(p) \approx \sum_{i=1}^{N}\Delta z_i^t(\alpha_i^{(0)} + \alpha_i^{(2)}p^2). \qquad (\text{C-4})
$$

Based on equation C-4, the depth shift between the plane-wave migration images with ray parameters of p and 0 is

$$
z_N^m(p) - z_N^m(p=0) = \left(\sum_{i=1}^{N}\alpha_i^{(2)}\right)p^2, \qquad (\text{C-5})
$$

which suggests that the moveout of the plane-wave CIG can be approximated by a parabola.

REFERENCES

Bickel, S. H., 1990, Velocity-depth ambiguity of reflection traveltimes: Geophysics, **55**, 266–276, doi: 10.1190/1.1442834.

Biondi, B., and P. Sava, 1999, Wave-equation migration velocity analysis: 69th Annual International Meeting, SEG, Expanded Abstracts, 1723–1726.

Biondi, B., and W. W. Symes, 2004, Angle-domain common-image gathers for migration velocity analysis by wavefield-continuation imaging: Geophysics, **69**, 1283–1298, doi: 10.1190/1.1801945.

Brandsberg-Dahl, S., M. V. de Hoop, and B. Ursin, 1999, Velocity analysis in the common scattering-angle/azimuth domain: 69th Annual International Meeting, SEG, Expanded Abstracts, 1715–1718.

Bunks, C., F. M. Saleck, S. Zaleski, and G. Chavent, 1995, Multiscale seismic waveform inversion: Geophysics, **60**, 1457–1473, doi: 10.1190/1.1443880.

Dai, W., 2012, Multisource least-squares migration and prism wave reverse time migration: Ph.D. thesis, The University of Utah.

Dai, W., and G. T. Schuster, 2013, Plane-wave least-squares reverse-time migration: Geophysics, **78**, no. 4, S165–S177, doi: 10.1190/geo2012-0377.1.

Dickens, T. A., and G. A. Winbow, 2011, RTM angle gathers using poynting vectors: 81st Annual International Meeting, SEG, Expanded Abstracts, 3109–3113.

Duquet, B., P. Lailly, and A. Ehinger, 2001, 3D plane wave migration of streamer data: 71st Annual International Meeting, SEG, Expanded Abstracts, 1033–1036.

Fomel, S., 2009, Velocity analysis using AB semblance: Geophysical Prospecting, **57**, 311–321, doi: 10.1111/j.1365-2478.2008.00741.x.

Hale, D., 2013, Dynamic warping of seismic images: Geophysics, **78**, no. 2, S105–S115, doi: 10.1190/geo2012-0327.1.

Huang, Y., X. Wang, and G. T. Schuster, 2014, Non-local means filter for trim statics: 84th Annual International Meeting, SEG, Expanded Abstracts, 3925–3929.

Jiao, J., P. L. Stoffa, M. K. Sen, and R. K. Seifoullaev, 2002, Residual migration-velocity analysis in the plane-wave domain: Geophysics, **67**, 1258–1269, doi: 10.1190/1.1500388.

Liu, F., D. W. Hanson, N. D. Whitmore, R. S. Day, and R. H. Stolt, 2006, Toward a unified analysis for source plane-wave migration: Geophysics, **71**, no. 4, S129–S139, doi: 10.1190/1.2213933.

Liu, F.D. N. Whitmore, D. W. Hanson, R. S. Day, and C. C. Mosher, 2004, The impact of reciprocity on prestack source plane wave migration: 74th Annual International Meeting, SEG, Expanded Abstracts, 1045–1048.

Luo, Y., and G. T. Schuster, 1991, Wave-equation traveltime inversion: Geophysics, **56**, 645–653, doi: 10.1190/1.1443081.

Ma, Y., and D. Hale, 2013, Wave-equation reflection traveltime inversion with dynamic warping and full-waveform inversion: Geophysics, **78**, no. 6, R223–R233, doi: 10.1190/geo2013-0004.1.

Mulder, W., and A. Ten Kroode, 2002, Automatic velocity analysis by differential semblance optimization: Geophysics, **67**, 1184–1191, doi: 10.1190/1.1500380.

Neidell, N. S., and M. T. Taner, 1971, Semblance and other coherency measures for multichannel data: Geophysics, **36**, 482–497, doi: 10.1190/1.1440186.

Nocedal, J., and S. Wright, 2006, Numerical optimization: Springer Science & Business Media.

Perrone, F., and P. Sava, 2013, Shot-domain 4D time-lapse velocity analysis using apparent image displacements: 83rd Annual International Meeting, SEG, Expanded Abstracts, 4932–4936.

Perrone, F., and P. Sava, 2015, Image-warping waveform tomography: Geophysical Prospecting, **63**, 1050–1069.

Perrone, F., P. Sava, C. Andreoletti, and N. Bienati, 2014, Linearized wave-equation migration velocity analysis by image warping: Geophysics, **79**, no. 2, S35–S46, doi: 10.1190/geo2012-0526.1.

Perrone, F., P. Sava, and J. Panizzardi, 2015, Wavefield tomography based on local image correlations: Geophysical Prospecting, **63**, 35–54, doi: 10.1111/1365-2478.12163.

Pratt, R. G., 1999, Seismic waveform inversion in the frequency domain. Part 1: Theory and verification in a physical scale model: Geophysics, **64**, 888–901, doi: 10.1190/1.1444597.

Rickett, J. E., and P. C. Sava, 2002, Offset and angle-domain common image-point gathers for shot-profile migration: Geophysics, **67**, 883–889, doi: 10.1190/1.1484531.

Ross, W. S., 1994, The velocity-depth ambiguity in seismic traveltime data: Geophysics, **59**, 830–843, doi: 10.1190/1.1443641.

Sava, P., and B. Biondi, 2004, Wave-equation migration velocity analysis. Part I: Theory: Geophysical Prospecting, **52**, 593–606, doi: 10.1111/j.1365-2478.2004.00447.x.

Sava, P., and S. Fomel, 2006, Time-shift imaging condition in seismic migration: Geophysics, **71**, no. 6, S209–S217, doi: 10.1190/1.2338824.

Sava, P. C., and S. Fomel, 2003, Angle-domain common-image gathers by wavefield continuation methods: Geophysics, **68**, 1065–1074, doi: 10.1190/1.1581078.

Shen, P., and W. W. Symes, 2008, Automatic velocity analysis via shot profile migration: Geophysics, **73**, no. 5, VE49–VE59, doi: 10.1190/1.2972021.

Stolk, C. C., and W. W. Symes, 2004, Kinematic artifacts in prestack depth migration: Geophysics, **69**, 562–575, doi: 10.1190/1.1707076.

Stork, C., 1992, Reflection tomography in the postmigrated domain: Geophysics, **57**, 680–692, doi: 10.1190/1.1443282.

Taner, M. T., and F. Koehler, 1969, Velocity spectradigital computer derivation applications of velocity functions: Geophysics, **34**, 859–881, doi: 10.1190/1.1440058.

Tarantola, A., 1984, Inversion of seismic reflection data in the acoustic approximation: Geophysics, **49**, 1259–1266, doi: 10.1190/1.1441754.

Vigh, D., and E. W. Starr, 2008, 3D prestack plane-wave full-waveform inversion: Geophysics, **73**, no. 5, VE135–VE144, doi: 10.1190/1.2952623.

Virieux, J., and S. Operto, 2009, An overview of full-waveform inversion in exploration geophysics: Geophysics, **74**, no. 6, WCC1–WCC26, doi: 10.1190/1.3238367.

Wang, X., W. Dai, Y. Huang, and G. T. Schuster, 2014, 3D plane-wave least-squares Kirchhoff migration: 84th Annual International Meeting, SEG, Expanded Abstracts, 3974–3979.

Whitmore, N. D., 1995, An imaging hierarchy for common-angle plane wave seismograms: Ph.D. thesis, University of Tulsa.

Xu, S., H. Chauris, G. Lambar, and M. Noble, 2001, Common angle migration: A strategy for imaging complex media: Geophysics, **66**, 1877–1894, doi: 10.1190/1.1487131.

Xu, S., Y. Zhang, and B. Tang, 2011, 3D angle gathers from reverse time migration: Geophysics, **76**, no. 2, S77–S92, doi: 10.1190/1.3536527.

Yilmaz, Ö., 2001, Seismic data analysis: SEG 1.

Zhang, Q., 2014, RTM angle gathers and specular filter (SF) RTM using optical flow: 84th Annual International Meeting, SEG, Expanded Abstracts, 3816–3820.

Zhang, S., Y. Luo, and G. Schuster, 2015, Shot- and angle-domain wave-equation traveltime inversion of reflection data: Theory: Geophysics, **80**, no. 4, U47–U59, doi: 10.1190/geo2014-0178.1.

Zhang, Y., and B. Biondi, 2013, Moveout-based wave-equation migration velocity analysis: Geophysics, **78**, no. 2, U31–U39, doi: 10.1190/geo2012-0082.1.

Zhang, Y., J. Sun, C. Notfors, S. H. Gray, L. Chernis, and J. Young, 2005, Delayed-shot 3D depth migration: Geophysics, **70**, no. 5, E21–E28, doi: 10.1190/1.2057980.